machines

MDPI

Article

Analysis of the Inertial Acceleration of a Shipborne Telescope Tracking Frame and Experimental Device Construction

Yingjie Li [1,2,*] and Libao Yang [2]

[1] Changchun Institute of Optics, Fine Mechanics and Physics, Chinese Academy of Sciences, Changchun 130033, China
[2] University of Chinese Academy of Sciences, Beijing 100049, China
* Correspondence: lyj990529@163.com; Tel.: +86-18226631105

Abstract

Shipborne photoelectric telescopes must consider the influence of the ship on structural stability during offshore operations. In this study, a 1.2 m shipborne photoelectric telescope tracking frame was investigated, and the inertial acceleration induced by hull motion was analyzed. Three ship motion modes were simplified as independent harmonic motions, and their motion equations and parameters were derived. The structural deformation under combined ship motions was evaluated by applying inertial loads through finite element analysis. The maximum deformations along the altitude axis parallel and perpendicular to the bow-stern line were both less than 0.09 mm, indicating negligible structural impact. A ship motion simulation system was developed and validated using an LMS modal analyzer. Modal analysis was performed to obtain the first six mode shapes, and sensor locations were optimized accordingly. The measured frequencies of the first six modes were 43.10, 47.47, 62.76, 74.52, 126.84, and 146.32 Hz, respectively, with the fundamental frequency exceeding the simulated value of 34.32 Hz.

Keywords: shipborne telescope; tracking frame; finite element analysis; simulation experimental device; LMS modal test

1. Introduction

An optical telescope is a set of optical, mechanical, and electronic technology that is integrated with photoelectric detection equipment, used for long-distance observation and for the monitoring and recording of missiles, rockets, and other flight targets [1]. Optical telescopes are widely used in military, aerospace, navigation, firefighting, and other fields, such as for target reconnaissance, fire strikes, and spacecraft detection [2,3]. With the rapid development of range optical technology, photoelectric telescopes from ground-based fixed installations have gradually evolved into mobile installations, such as photoelectric telescopes, by installing in vehicles, ships, aircraft, and even missile cargo satellites and other mobile platforms [4,5]. Shipborne equipment can provide more flexible station deployment than ground-based equipment [6]. However, ship motions due to wave impacts usually cause severe vibration damage to the equipment. When a surveying ship is traveling, the equipment fixed on the deck will experience a large inertial acceleration with the ship motions [7,8]. To deeply understand the influence of waves on telescope equipment under shipborne conditions, the inertial acceleration of shipborne equipment caused by the sailing of the surveying ship needs to be analyzed [9].

Finite element analysis is an effective method to solve this kind of problem [10]. This method models the excitation environment through mechanical simulations of the

Academic Editor: Zhuming Bi

Received: 8 August 2026
Revised: 2 September 2026
Accepted: 4 September 2026
Published: 15 September 2026

structure, allows the performance of the system to be compared and analyzed to determine whether it meets the design requirements [11]. Foreign finite element analysis technology for large-aperture telescope is indeed in a leading position [12]. For example, the National Large Telescope of Japan has carried out finite element analysis of dynamic and static wind loads [13]. The seismic frequency response of the Very Large Telescope at The European Southern Observatory was simulated and analyzed at the geographic location of the installation [14]. Simulations of the Giant Magellan Telescope have been carried out in order to study the effect of the wind load on the spliced primary mirror using the wind pressure data collected from tests [15]. In China, many scholars have applied finite element technology and carried out finite element simulation work. Feng performed static analysis of the telescope based on temperature and mechanics [16]. Hu proposed a lightweight sheet-metal welded structure for the 30 m Future Giant Telescope (CFGT) and performed finite element modeling and analysis [17]. Zuo H used simulation software to thermally analyze the focal plane of the LAMOST telescope, examined the temperature characteristics [18].

In addition to global deformation and vibration characteristics, the local stress distribution is also important for evaluating the structural integrity of mechanical systems. Stress concentrations can occur around geometric discontinuities and structural connections, making these regions more susceptible to fatigue damage under repeated or dynamic loading [19,20]. Therefore, identifying critical stress regions is important for evaluating the safety and reliability of a telescope tracking frame subjected to shipborne loads.

However, previous studies on shipborne telescope tracking frames have mainly focused on structural deformation, modal characteristics, and stability evaluation under prescribed loads [21], with limited attention to the conversion of ship motion into equipment-level inertial loads and the identification of critical stress regions [22]. In this study, simplified ship-motion modeling, equivalent inertial loading, and finite element analysis are combined.

This article briefly introduces the tracking frame structure and the ship motions and analyzes the inertial acceleration induced by ship motions. The complex ship motions are approximated by independent simple harmonic motions, and the resulting inertial acceleration is applied as an equivalent loading condition to simplify the dynamic analysis. Meanwhile, a ship motion simulation experimental device is designed and constructed. The experimental results are used to verify the proposed method. Furthermore, the stress distribution of the tracking frame is analyzed to identify the critical stress regions under shipborne conditions, providing a basis for evaluating the structural integrity of the tracking frame.

2. Structure and Finite Element Model of Tracking Frame

2.1. Structure

The tracking frame is the foundation and core of a telescope. In this paper, the tracking frame is an altitude–azimuth mount. The frame accomplishes the altitude and azimuth motions required for observation and provides a mechanical interface and carrying platform for the optoelectronic system components [23]. An altitude–azimuth ground-based telescope consists of an azimuth axis system and an altitude axis system. The axis system perpendicular to the ground is called the azimuth axis system, The one parallel to the ground is called the altitude axis system, both of which are perpendicular to each other. This type of tracking frame is left and right symmetric, with a better force condition and high reliability, and it is suitable for shipborne large-caliber systems. The large structural elements of the tracking frame are composed of a pedestal, a turntable, left and right columns, and a cross from low to high [24,25], which carries the primary mirror chamber as well as the secondary mirror chamber, as shown in Figure 1.

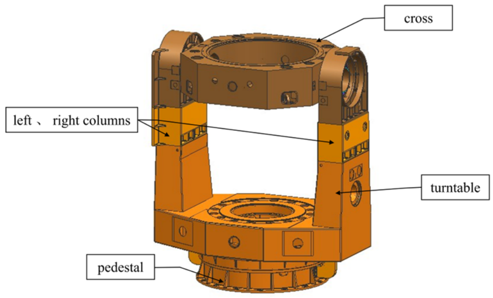

Figure 1. Structure model of the tracking frame.

2.2. Finite Element Model

The structure of the device was simplified based on the stress conditions of the tracking frame. Elements such as rounded corners, chamfers, bolts, and threaded holes that were unfavorable to mesh delineation could be omitted, and those that would not affect the analysis results could also be omitted. Moreover, each large structural component of the tracking frame was simplified to reduce the model complexity [26,27]. On the basis of the simplified model, mesh division was carried out, and the relationships between each structural component and the material properties of each structural component were defined based on the working mode of the equipment. The finite element model of the tracking frame is shown in Figure 2. The finite element model of the tracking frame contained 13,225 elements, predominantly hexahedral elements. The tracking frame was constructed from welded steel plates, with the corresponding material properties assigned according to the material specifications. The structural components were modeled based on their actual assembly and welding conditions. The base was constrained at the twelve anchor-bolt locations to reproduce the actual installation conditions, and a mesh-independence analysis confirmed the adequacy of the selected mesh.

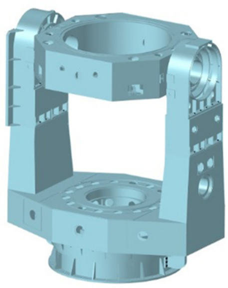

Figure 2. Finite element model of the tracking frame.

3. Ship Motions

A ship sailing in still water or with waves around a certain equilibrium position undergoes periodic reciprocating are called ship motions. The ship motions mainly include rolling, pitching, yawing, swaying, surging, and heaving [28]. Its specific motion form is shown in Figure 3.

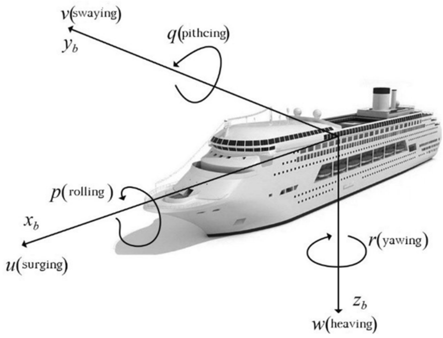

Figure 3. Schematic diagram of the motions of the six degrees of freedom of ship motions.

There are six main types of ship motions:

1. Rolling: the periodic oscillating motion of a ship about its longitudinal axis (the fore-and-aft direction);
2. Pitching: the periodic oscillating motion of a ship about its transverse axis (the lateral direction);
3. Yawing: the periodic up-and-down motion of a vessel about its vertical axis (the fore-and-aft direction);
4. Swaying: the periodic back-and-forth motion of a vessel about its transverse axis (the lateral direction);
5. Surging: the periodic reciprocating motion of a vessel about its longitudinal axis (the fore-and-aft direction of the vessel);
6. Heaving: the periodic reciprocating motion of a vessel about its vertical axis (the up-and-down direction of the vessel).

Although a ship has six degrees of freedom, this study focuses on roll, pitch, and heave, which are considered the primary motions governing the inertial excitation of the shipborne telescope tracking frame [29,30]. Surge, sway, and yaw are neglected as a modeling simplification because their effects are outside the scope of the present structural response analysis. It should be noted that the actual six-DOF ship motions is governed by the sea state, hull geometry, wave heading, ship speed, loading condition, and hydrodynamic characteristics; therefore, the independent harmonic representation adopted in this study is intended as a simplified representation of the shipborne excitation rather than a complete prediction of the real ship motion.

The shipborne tracking frame may experience loose connections, excessive deformation of the azimuth or altitude axis, excessive local structural stress, and other problems affecting the safe and normal operation of the equipment when ship motions resonance occur [31,32].

3.1. Ship Motion Analysis

When a ship is sailing at sea, it usually undergoes oscillating motion due to wave excitation, such motion can be approximated as simple harmonic motion or as a superposition of several harmonic components [33]. In this study, the ship motions are simplified as harmonic excitations. The roll and pitch frequencies are 0.10 Hz and 0.067 Hz, respectively, which are much lower than the first natural frequency of the structure. Therefore, significant resonance and dynamic amplification are unlikely, and the ship-induced inertial loads can be reasonably treated as quasi-static loads [34].

To facilitate the study of the ship motion characteristics, a simple harmonic equation of motion is introduced to describe the ship motion for its degrees of freedom, and the following assumptions are made at the macroscopic level [35]:

1. The amplitude of the wave is less than the wavelength of the overall wave;
2. The amplitude of the ship motions is less than the wavelength of the wave;
3. Waves have a planar form of the wave front in the direction of propagation;
4. The center of oscillation of the ship remains constant when the ship is subjected to oscillations under wave action;
5. The ship motions for each degree of freedom are considered to be independent of each other;
6. The center of oscillation is located close to the ship's center of gravity.

As a result, the three degree-of-freedom motions that can have the greatest impact on shipborne equipment: rolling, pitching, and heaving, can be analyzed by replacing the ship motions with an independent simple harmonic motion function, utilizing a mathematical approach instead of complex physical motions.

3.2. Parameter Calculations

The dimensions of the vessel are approximately: length $\times$ beam $\times$ height $\approx$ 222 m $\times$ 25 m $\times$ 40 m.

3.2.1. Ship Rolling

An oscillating differential equation is established to measure the ship rolling motion. When the ship undergoes rolling motion around the center of gravity of the hull, the rolling motion is approximated as a forced vibration of a spring. When the spring makes an unconstrained forced vibration at a fixed connection point, the simple harmonic equation of motion of the spring is as follows [36–38]:

$$y(t) = A \sin \omega_0 t \tag{1}$$

where A represents the maximum vibration amplitude of the spring, and ω_0 represents the vibration frequency of the spring.

Suppose the instantaneous displacement is x (m), Based on Equation (1), the differential equation for the motion obtained from Newton's second law is as follows:

$$m\ddot{x} + 2\zeta\dot{x} + kx = kA \sin \omega t \tag{2}$$

where ζ is the damping coefficient, and k is the spring constant.

The differential equation for the ship rolling motion is established as

$$M_\varphi \ddot{\varphi} + 2\zeta_\varphi \dot{\varphi} + C_\varphi \varphi = F_\varphi \tag{3}$$

where φ denotes the ship rolling inclination angle, M_φ denotes the ship rolling inertia force coefficient, ζ_φ denotes the ship rolling damping coefficient, C_φ denotes the ship rolling equivalent restoring force coefficient, and F_φ denotes the transverse rolling wave disturbing force.

The following is obtained according to the principle of dynamic balancing:

$$\left(J_\varphi \varphi + \Delta J_\varphi\right) \varphi'' + VH_\varphi = 0 \tag{4}$$

where J_φ denotes the moment of inertia of the measurement vessel around the center of inertia spindle, ΔJ_φ denotes the additional moment of inertia, and H_φ denotes the height of the cross-sectional steady center. J_φ can be calculated using the following formula:

$$J_\varphi = \frac{V\left(b^2 + Z_g^2\right)}{12g} \tag{5}$$

Equation (4) is rewritten to obtain the following:

$$\varphi'' + \frac{VH_\varphi}{J_\varphi + \Delta J_\varphi} = 0 \tag{6}$$

The rolling intrinsic frequency n_φ is given as follows:

$$n_\varphi^2 = \frac{VH_\varphi}{J_\varphi + \Delta J_\varphi} \tag{7}$$

The approximate intrinsic period of the rolling of the surveying ship is

$$T_\varphi = \frac{2\pi}{n_\varphi} = 2\pi\sqrt{\frac{J_\varphi + \Delta J_\varphi}{VH_\varphi}} \tag{8}$$

According to Equation (8), the size of the intrinsic period and the size of the rolling inclination do not change with time but depend on the ship's intrinsic attributes.

Substituting the moment of inertia into Equation (3) yields

$$\left(J_\varphi + \Delta J_\varphi\right)\ddot{\varphi} + 2\zeta_\varphi\dot{\varphi} + C_\varphi\varphi = F_\varphi \tag{9}$$

The main disturbance moment of the rolling wave $F_\varphi = VH_\varphi a_\varepsilon sin\omega_\varphi t$, where a_ε denotes the inclination amplitude of the wave, and ω_φ denotes the rolling circle frequency.

Substituting F_φ into Equation (9) yields

$$\left(J_\varphi + \Delta J_\varphi\right)\ddot{\varphi} + 2\zeta_\varphi\dot{\varphi} + C_\varphi\varphi = VH_\varphi a_\varepsilon \sin\omega_\varphi t \tag{10}$$

Considering the waves as plane simple harmonic waves, the ship rolling is a simple harmonic motion with a special solution:

$$\varphi = \varphi_{\max}\sin\left(\omega_\varphi t + \varepsilon_\varphi\right) \tag{11}$$

where φ_{max} denotes the maximum rolling inclination, ε_φ denotes the phase difference.

In Figure 4, where M denotes the self-weight of the device, y denotes the lateral distance of the center of gravity of the device from the center of the rolling motion, z denotes the longitudinal distance of the center of gravity of the device from the center of the rolling motion, and r_φ denotes the distance of the center of gravity of the device from the center of the rolling motion. From Equations (7) and (12), the equation of motion for the ship rolling can be obtained as:

$$\varphi = \varphi_{\max}\sin\left(\frac{2\pi}{T_\varphi}t + \varepsilon_\varphi\right) \tag{12}$$

where φ_{max} denotes the maximum transverse angle of ship rolling, T_φ denotes the period of ship rolling, and ε_φ denotes the phase difference.

The angular acceleration is

$$\varphi'' = -\frac{4\pi^2 \cdot \varphi_{\max}}{T_\varphi^2} \cdot \sin\left(\frac{2\pi \cdot t}{T_\varphi} + \varepsilon_\varphi\right) \tag{13}$$

When the ship is rolling, the equipment fixed on the deck swings in a small range of the cross section to undergo circular motion. The tangential acceleration calculation formula is as follows:

$$a_\varphi = r_\varphi \cdot \varphi'' \tag{14}$$

At this point, $r_\varphi = z$. The tangential force generated by the device from a short-range circular motion within the cross section of the surveying ship is

$$F_\varphi = M \cdot r_\varphi \cdot \varphi'' = M \cdot z \cdot \varphi'' \tag{15}$$

The horizontal and vertical components of the tangential force generated by the ship rolling in the cross section are respectively

$$F_{\varphi y} = F_\varphi \cdot \cos\varphi = M \cdot z \cdot \varphi'' \cdot \cos\varphi \tag{16}$$

$$F_{\varphi z} = F_\varphi \cdot \sin\varphi = M \cdot z \cdot \varphi'' \cdot \sin\varphi \tag{17}$$

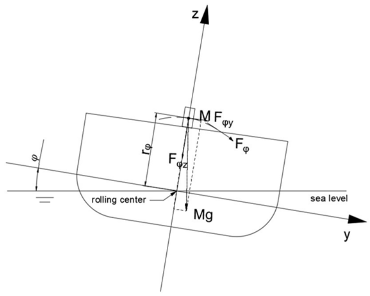

Figure 4. Vector diagram of the tracking frame inertial forces during ship rolling.

According to the IMO (International Maritime Organization) requirements, most ships are in danger if their rolling inclination exceeds 35°, and this is even more demanding for surveying ships.

3.2.2. Ship Pitching

Modeling the ship pitching is similar to modeling the ship rolling. The derivation is omitted. Figure 5 shows the forces during ship pitching. In the figure, M denotes the self-weight of the device, x denotes the lateral distance of the center of gravity of the device from the center of the pitching, z denotes the pitching of the center of gravity of the device from the center of the pitching, and r_θ denotes the distance of the center of gravity of the device from the center of the pitching, i.e., the radius of the pitching.

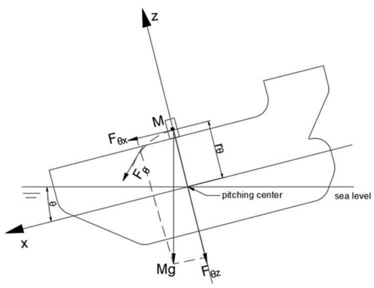

Figure 5. Vector diagram of the tracking frame inertial forces during ship pitching.

At this point,

$$r_\theta = z \tag{18}$$

The tangential force in the longitudinal section of the surveying ship generated by the short-range circular motion of the device is

$$F_\theta = M \cdot r_\theta \cdot \theta'' = M \cdot z \cdot \theta'' \tag{19}$$

The horizontal and vertical components of the tangential force generated by the ship pitching in the cross section are respectively

$$F_{\theta x} = F_\theta \cdot \cos\theta = M \cdot z \cdot \theta'' \cdot \cos\theta \tag{20}$$

$$F_{\theta z} = F_\theta \cdot \sin\theta = M \cdot z \cdot \theta'' \cdot \sin\theta \tag{21}$$

In the IMO standard, the maximum pitching angle is not specified. However, taking into account the special characteristics of the surveying ship, 20° was taken as the maximum pitching angle.

3.2.3. Ship Heaving

The derivation of the equations of motion for rolling and pitching can also be used in the derivation of the equations for ship heaving. The difference is that the rolling and pitching are circular, while the heaving is linear with respect to the rolling and pitching motion, as shown in the Figure 6. No formula derivation is presented here.

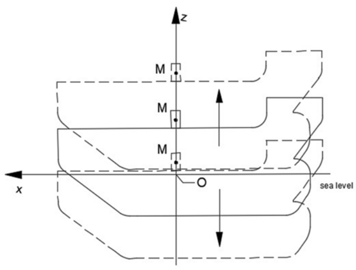

Figure 6. Schematic diagram of the tracking frame when the surveying ship is heaving.

The equation of motion for the ship heaving can be obtained as

$$z = z_{\max} \cos\left(\frac{2\pi}{T_z} t + \varepsilon_z\right) \tag{22}$$

The heaving acceleration was calculated to be about 0.3 m/s^2. After calculating the three kinds of ship motion parameters, their respective formulas were used to calculate the value of the inertial acceleration, which was required for the subsequent simulation.

Based on the IMO International Code on Intact Stability (2008 IS Code, as amended) and previous studies on survey vessel motion [39], a roll angle of 30° with a period of 10 s was selected as a representative severe condition. As no specific pitch limit is prescribed by IMO, a pitch angle of 20° and a period of 15 s were adopted as conservative conditions. The corresponding heave parameters were calculated using the above equations and are listed in Table 1.

Table 1. Ship motion parameters.

Motion Mode	Maximum Tilt Angle/°	Oscillating Period/s
Rolling	30	10
Pitching	20	15
Heaving	/	/

4. Simulations

4.1. Altitude Axis Parallel to the Direction of Bow and Stern Line

The center-of-gravity coordinates of the tracking frame were obtained from the three-dimensional model and defined in the global coordinate system. The previously calculated inertial accelerations and gravitational acceleration were then applied to the finite element model as body acceleration loads, while the base was fully constrained. The stress distribution of the tracking frame was subsequently calculated, and the corresponding stress contours were obtained.

The inertial accelerations due to transverse and longitudinal oscillations, as well as pendular oscillations, were applied to the tracking frame to obtain the deformation diagram shown in Figure 7. The largest area of deformation of the tracking frame under ship loading was concentrated in the upper half of the tracking frame, which was mainly manifested in the deformation of the cross and the left and right columns. The largest stress was concentrated in the holes of the ground bolts of the pedestal.

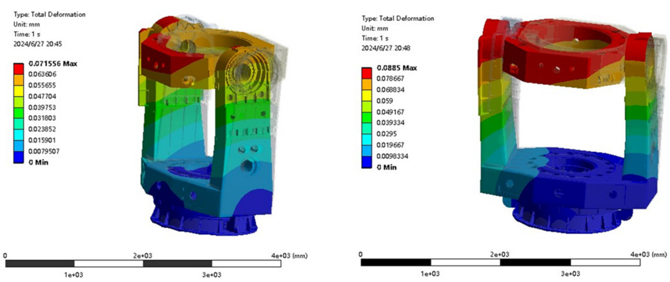

(**a**) (**b**)

Figure 7. Deformation cloud maps under ship oscillating: (**a**) Parallel. (**b**) Perpendicular.

4.2. Altitude Axis Perpendicular to the Direction of Bow and Stern Line

The same combination was considered in the same direction as the altitude axis parallel to the bow and stern lines. The deformation of the tracking frame under these motion states is shown in Figure 8. Similarly to the first case, the maximum area of deformation of the tracking frame under shipload was concentrated in the upper half of the frame, which was manifested by the deformation of the cross and the left and right columns, and the maximum stress was also concentrated at the holes of the ground bolts in the pedestal. In both cases, the maximum deformation was less than 0.09 mm, the distance between the left and right sides of the telescope is about 2 m. The maximum deformation of the tracking frame under the considered shipborne loading conditions was less than 0.09 mm. Rather than indicating that the effect of ship motion can be completely neglected, this result demonstrates that the deformation induced by the considered inertial loads remains relatively limited. Considering the structural dimensions and functional requirements of the tracking frame, the calculated deformation is sufficiently small to maintain the overall structural stability and support normal tracking operation. Therefore, under the investigated ship motion conditions, the tracking frame exhibits adequate structural stiffness for shipboard operation.

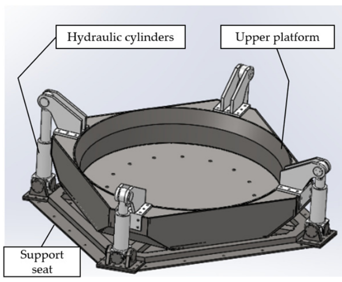

Figure 8. Schematic diagram of the experimental device.

Among the general six-degree-of-freedom motions of ships, rolling has the greatest impact on shipborne equipment because the amplitude of the rolling motion is usually larger and more frequent compared to other ship motions, such as pitching and heaving. This causes the shipborne tracking frame to be subjected to large inertial forces and dynamic loads during rolling, which affects the safe operation of the equipment. In addition, the rolling motion leads to a large port and starboard tilt of the surveying ship, which changes the distribution of the center of gravity inside the hull and increases the uncertainty of the forces on the shipborne equipment.

To improve the effect of the ship rolling on the shipborne equipment, several common methods are summarized as follows:

1. Improvement of the shape and structure of the surveying ship to increase the stability of the ship and reduce the rolling amplitude;
2. Advanced stability control systems or automatic stabilizer fins (oscillating reduction fins) to reduce the ship rolling;
3. Consideration of how the equipment is arranged and secured so that it is better able to resist the effects of rolling on the equipment, e.g., by increasing the number of support and securing points for the equipment;
4. Utilization of technical means, such as active damping systems or dampers, to dampen the shipborne equipment in order to reduce the effects of rolling on the equipment.

5. Ship Motion Simulation Experimental Device

To ensure the stability and reliability of the tracking frame in the ship motions and to verify the accuracy of the finite element model, it was necessary to conduct real ship experiments to evaluate the mechanical structure performance of the tracking frame. The actual ship experiment involved huge labor costs, material resources, financial resources, and time consumption. To reduce the cost and risk, a ship motion simulation experimental device was designed and built to simulate the effect of ship motions on the tracking frame.

5.1. Main Structure

The main structure of the experimental device is a frame structure as shown in Figure 8. After the main body was welded, it was first de-stressed and annealed to eliminate welding stress, and then it was processed. The structure is described as follows:

1. The support seat was connected to the ground for fixing, supporting, and preventing overturning. Crosshair joints were provided on top of the support seat, and the upper ball seat swung relative to the bottom crosshair joints and served as a limit. The support seat was fixed to the ground by ground bolts;
2. Four hydraulic cylinders were installed with a certain taper to ensure the stability of the equipment, in which the diagonal cylinders were synchronized with positive and negative expansion and contraction action, which could be controlled by the hydraulic valve handle and frequency converter for point and speed control;
3. The upper platform was used to carry the connection to the tracking frame during the experiment, as shown in Figure 9.

Figure 9. Actual diagram of the experimental device.

5.2. Modal Analysis and Test

5.2.1. Modal Analysis

The purpose of the modal analysis of the tracking frame was to obtain the intrinsic frequency of the tracking frame, to determine the weak position of the structure, to provide a theoretical basis for the subsequent design, and to be able to guide the modal test [40]. The altitude bearing, azimuth bearing, and bolts were simplified as rigid connections, and the pedestal was fully restrained. The first six orders of modal frequencies of the tracking frame were obtained, as shown in Table 2, and the first six orders of vibration patterns are shown in Figure 10.

Table 2. First six natural frequencies and mode shapes of the tracking frame.

Order	Frequency/Hz	Mode Shapes
1	40.57	Integral translation along the Y-axis
2	43.02	Integral translation along the X-axis
3	62.50	Integral torsion around the Z-axis
4	78.96	Relative translation of the whole body along the X-axis
5	135.56	Relative translation of the whole body along the X-axis
6	148.12	Cross twisting around the altitude axis

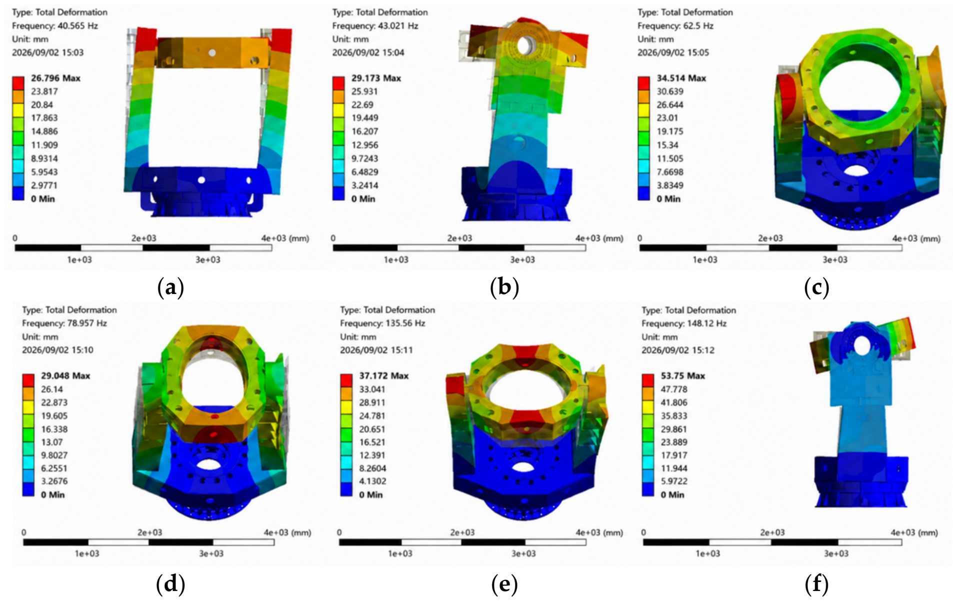

Figure 10. Modal shapes for first six orders: (**a**) 1st-order modal shape. (**b**) 2nd-order modal shape. (**c**) 3rd-order modal shape. (**d**) 4th-order modal shape. (**e**) 5th-order modal shape. (**f**) 6th-order modal shape.

5.2.2. LMS Modal Test

The modes were tested using a hammering method with the 16 ground bolts of the pedestal as fixed constraints.

- Test instruments:
  (a) 16-channel LMS modal analyzer;
  (b) Five three-way accelerometers;
  (c) 086D20 force hammer.
- Specific implementation programs and processes

The specific steps were as follows:

1. Geometric modeling: The tracking frame was treated as five nodes. The nodes were connected to a frame diagram, and bond accelerometers were positioned at each point location, as shown in Figure 11;
2. Channel settings: Properties such as the sensor name and sensor sensitivity were defined;
3. Sensor calibration: The sensors were arranged based on the modal analysis results in Section 5.2.1, as shown in Figures 11 and 12. They were mainly arranged in the left and right columns and at the turntable position;
4. Hammer oscillator: The range of each channel was set by hammering the structure within the test range. The appropriate range could provide more accurate test results. The sampling frequency was set to 1024 Hz. A hammering test was performed to select the rotary table fork arm side position, as shown in Figure 13;
5. Hammering setup: Parameters such as the location of the impact point, the size of the impact force, and the form of the impact signal were set. The test was stimulated six times;
6. Measurement: The vibration response data of the structure under impact excitation were recorded by vibration sensors to obtain the vibration modes and frequency response of the structure. The specific implementation process is shown in Figure 14.

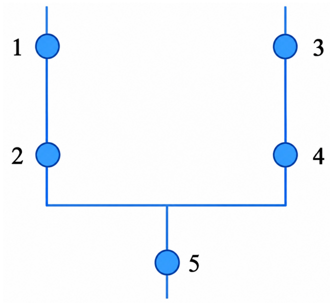

Figure 11. Sensor position.

(**a**) (**b**) (**c**)

Figure 12. Specific locations of the sensors: (**a**) Left column sensors. (**b**) Pedestal sensor. (**c**) Right column sensors.

As shown in Figure 15, Modal testing showed that the first six natural frequencies of the tracking frame were 43.10, 47.47, 62.76, 74.52, 126.84, and 146.32 Hz, respectively, as shown in Table 3, with discrepancies of less than 10% compared with the corresponding numerical results. The good agreement between the experimental and simulated results demonstrates the validity of the finite element model and confirms that the structural design of the tracking frame satisfies the stability requirements for shipboard operation. These results also provide a reliable experimental basis for further experimental investigations of the tracking frame under shipborne operating conditions.

Figure 13. Position of force hammer strike.

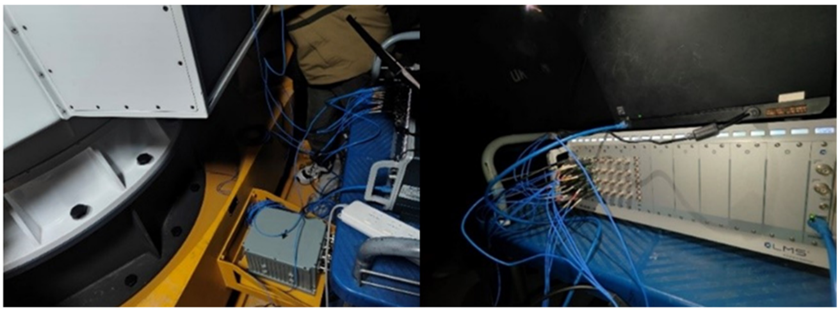

(**a**) (**b**)

Figure 14. Specific implementation process: (**a**) Sensor connection. (**b**) Linkage arrangement.

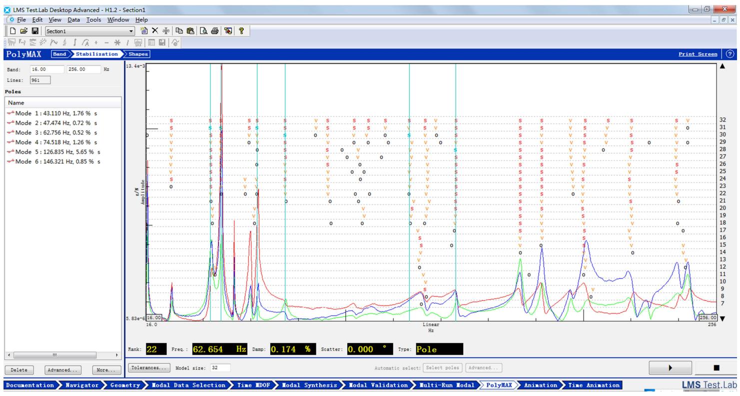

Figure 15. Modal test results.

Table 3. Calculated modal relative to actual modal error.

Order	Actual Modality /Hz	Simulate Modalities /Hz	Relative Error /%
1	43.10	40.57	5.87
2	47.47	43.02	9.37
3	62.76	62.50	0.42
4	74.52	78.96	5.32
5	126.84	135.56	6.43
6	146.32	148.12	1.22

https://doi.org/10.3390/machines14091047

1. Increased stiffness: The inclusion of the experimental device increased the stiffness of the overall system by providing additional support or introducing constraints that increased the overall stiffness of the system;
2. Altered mass distribution: The inclusion of the experimental device may have also altered the mass distribution of the system, resulting in an elevated fundamental frequency. If the mass of the tilt experimental device was concentrated in the region that affected the first-order modes, then it would result in an elevated first-order frequency;
3. Influenced constraints: The inclusion of the experimental device may have changed the constraints of the system. This may have resulted in the structure being constrained differently during vibration, thus affecting the frequency of the vibration modes;
4. Introduced nonlinear effects: The experimental device itself may have introduced some nonlinear effects such as friction and contact nonlinearity. These effects could lead to changes in the vibration modes, raising the first-order frequency.

Moreover, the fundamental frequencies of the tracking frame and experimental device were close to the standard industrial frequency of the power system. In this frequency range, many control systems are simpler to design and adjust. In summary, the experimental conditions in this paper satisfied the strength and stiffness requirements as well as the ability to balance the system performance, control requirements, and practical applications. Therefore, the experimental device and method in this paper are reasonable and feasible for simulating ship motion experiments.

6. Results

In this study, the inertial acceleration experienced by the tracking frame of a shipborne 1.2 m aperture photoelectric telescope during the voyage of a surveying ship was analyzed. A finite element model of the tracking frame was established. The ship motion was briefly introduced, and the three ship motions of rolling, pitching, and heaving, which have the greatest influence on the shipborne equipment, were approximated as short-range circular motion around the center of gravity of the ship. Equations of motion of the ship oscillating for the three degrees of freedom were established, and the corresponding parameters of the inertial acceleration were subsequently obtained. The tracking frame was investigated during the joint action of these three ship motion states. Finite element analysis of the tracking frame under the combined effect of these three ship motion states was carried out by considering the directions parallel and perpendicular to the bow and stern lines. The maximum deformation of the tracking frame was less than 0.09 mm. Finally, a ship motion simulation experimental device was designed and constructed to carry out the initial preparatory work for the simulation experiment of the tracking frame for the ship motion simulation. The main structure was described in detail. Finally, the validity of the ship motion simulation experimental conditions was preliminarily verified by modal tests.

Author Contributions: Conceptualization, Y.L. and L.Y.; methodology, Y.L. and L.Y.; software, Y.L.; validation, Y.L. and L.Y.; formal analysis, Y.L.; investigation, Y.L.; resources, L.Y.; data curation, Y.L.; writing—original draft preparation, Y.L.; writing—review and editing, Y.L.; visualization, Y.L.; supervision, L.Y. All authors have read and agreed to the published version of the manuscript.

Funding: This research received no external funding.

Data Availability Statement: The authors state that no new data was created, and all the data came from their own experiments and simulations.

Acknowledgments: The authors have reviewed and edited the output and take full responsibility for the content of this publication.

Conflicts of Interest: The authors declare no conflicts of interest.

References

1. Bely, P.Y. *The Design and Construction of Large Optical Telescopes*; Springer: Berlin/Heidelberg, Germany, 2003.
2. Ali, R.; Liu, R.; He, Y.; Nayyar, A.; Qureshi, B. Systematic review of dynamic multi-object identification and localization: Techniques and technologies. *IEEE Access* **2021**, *9*, 122924–122950. [CrossRef]
3. Nie, T.; Zhang, W.; Chai, M. Fusion positioning method of optical measuring equipment and GNSS. In Proceedings of the Fifth Symposium on Novel Optoelectronic Detection Technology and Application, Xi'an, China, 24–26 October 2019; pp. 208–216.
4. King, H.C. *The History of the Telescope*; Courier Corporation: North Chelmsford, MA, USA, 2003.
5. McKechnie, T.S. History of the Telescope and Its Remarkable Contribution to Scientific Discovery (and the 400-Year Journey from Galileo to a Rigorous General Theory of Imaging Through Earth's Turbulent Atmosphere). In *General Theory of Light Propagation and Imaging Through the Atmosphere*; Springer: Berlin/Heidelberg, Germany, 2022; pp. 1–22.
6. Kellett, J.; Dawber, W.; Wallace, W.; Branson, J. Multifunction maritime radar and RF systems—Technology challenges and areas of development. *IEEE Aerosp. Electron. Syst. Mag.* **2021**, *37*, 6–20. [CrossRef]
7. Ji, C.; Zhang, C. Research on Selection of Base for Impact Assessment of Shipborne. In Proceedings of the MARINE VIII: Proceedings of the VIII International Conference on Computational Methods in Marine Engineering, Göteborg, Sweden, 13–15 May 2019; pp. 556–567.
8. Gu, D.; El-Sheimy, N.; Hassan, T.; Syed, Z. Coarse alignment for marine SINS using gravity in the inertial frame as a reference. In Proceedings of the 2008 IEEE/ION Position, Location and Navigation Symposium, Monterey, CA, USA, 5–8 May 2008; pp. 961–965.
9. Chhoeung, S.; Hahn, A. Approach to estimate the ship center of gravity based on accelerations and angular velocities without ship parameters. *J. Phys. Conf. Ser.* **2019**, *1357*, 012028. [CrossRef]
10. Bhavikatti, S. *Finite Element Analysis*; New Age International: New Delhi, India, 2005.
11. Kurowski, P.M. *Finite Element Analysis for Design Engineers*; SAE International: Warrendale, PA, USA, 2022.
12. Cheng, J. *The Principles of Astronomical Telescope Design*; Springer: New York, NY, USA, 2009.
13. Itoh, N.; Mikami, I.; Noguchi, T.; Shimizu, Y.; Yamashita, Y.; Sovka, J.; McLaren, R.A.; Erasmus, D.A. Mechanical structure of JNLT: Analysis of mirror deflection due to wind loading. In *Advanced Technology Optical Telescopes IV*; SPIE: Warrendale, PA, USA, 1990; pp. 866–877.
14. Padovani, P.; Cirasuolo, M. The extremely large telescope. *Contemp. Phys.* **2023**, *64*, 47–64. [CrossRef]
15. Kan, F.W.; Eggers, D.W. Wind vibration analyses of giant Magellan telescope. In *Modeling, Systems Engineering, and Project Management for Astronomy II*; SPIE: Warrendale, PA, USA, 2006; pp. 271–283.
16. Shouwei, H.; Yong, Z.; Yuefei, W.; You, W. Concept design for the main structure of 30 m Chinese Future Giant Telescope. *Opto-Electron. Eng.* **2022**, *49*, 210402.
17. Zuo, H.; Yang, D.; Li, G. The finite element modeling and thermal analysis of the special focal plane of LAMOST. In *Ground-Based and Airborne Telescopes III*; SPIE: Warrendale, PA, USA, 2010; pp. 1901–1909.
18. Ding, S.; San, X.; Gao, S.; Ni, Y.; Wang, J. Laser communication pointing errors caused by bending deformation of the altitude axis of a T-shaped altitude-azimuth mount. *Appl. Opt.* **2019**, *58*, 8141–8147. [CrossRef] [PubMed]
19. Susmel, L.; Taylor, D. Fatigue design in the presence of stress concentrations. *J. Strain Anal. Eng. Des.* **2003**, *38*, 443–452. [CrossRef]
20. Taylor, D.; Bologna, P.; Knani, K.B. Prediction of fatigue failure location on a component using a critical distance method. *Int. J. Fatigue* **2000**, *22*, 735–742. [CrossRef]
21. Li, Y.; Yang, L.; Chen, T. Stability analysis of a shipborne large aperture telescope tracking rack. *J. Mech. Strength* **2025**, *47*, 110–118.
22. Li, W.; Tang, Y.; He, Y. Simulation and experimental analysis of critical stress regions of deep-water annular blowout preventer. *Eng. Fail. Anal.* **2019**, *106*, 104161. [CrossRef]
23. Kingsley, J.; Strittmatter, P.; Gonzales, K.; Connors, T.; Kingsley, B.; Jannuzi, B.; Yoshii, Y.; Minezaki, T. A domeless, mobile 2-meter telescope. In *Ground-Based and Airborne Telescopes VIII*; SPIE: Warrendale, PA, USA, 2020; pp. 704–716.
24. Krysiak, B.; Pazderski, D.; Kozłowski, S.; Kozłowski, K. High Efficiency Direct-drive Mount for Space Surveillance and NEO Applications. *Publ. Astron. Soc. Pac.* **2020**, *132*, 095002. [CrossRef]
25. Wang, C.-J.; Bai, J.-M.; Fan, Y.-F.; Mao, J.-R.; Chang, L.; Xin, Y.-X.; Zhang, J.-J.; Lun, B.-L.; Wang, J.-G.; Zhang, X.-L.; et al. Lijiang 2.4-meter Telescope and its instruments. *Res. Astron. Astrophys.* **2019**, *19*, 149. [CrossRef]
26. Liu, R.; Zhang, H.; Wang, X.; Gao, Q.; Liu, Z.; Yu, Y.; Wang, Q. Dynamic modeling and vibration characteristics analysis of a large-scale photoelectric theodolite tracking frame. *Machines* **2022**, *10*, 1150. [CrossRef]
27. Ereiz, S.; Duvnjak, I.; Jiménez-Alonso, J.F. Review of finite element model updating methods for structural applications. *Structures* **2022**, *41*, 684–723. [CrossRef]

28. Cheng, M.; Jiang, W.; Tao, B.; Zheng, X.; Guo, L. Influence of Ship Swaying motion on performance of Maritime Laser Communications in the Turbulence. In Proceedings of the 2021 13th International Symposium on Antennas, Propagation and EM Theory (ISAPE), Zhuhai, China, 1–4 December 2021; pp. 1–3.
29. Ibrahim, R.; Grace, I. Modeling of ship roll dynamics and its coupling with heave and pitch. *Math. Probl. Eng.* **2010**, *2010*, 934714. [CrossRef]
30. Nan, G.; Zhang, C.; Zhang, B.; Yang, S.; Hu, J. Dynamic Analysis of the Rod-Traction System for Ship-Borne Aircraft Under High Sea States. *Aerospace* **2026**, *13*, 107. [CrossRef]
31. Sun, H.; Wang, C.; Pang, W. Modeling and simulation of ship swaying attitude based on linear system theory. In *Complex, Intelligent, and Software Intensive Systems*; Springer: Cham, Switzerland, 2018; pp. 695–703.
32. Xu, X.; Li, Z.; Wang, L.; Yao, S.; Li, X. Modelling, Simulation and Analysis of the Crane Ship Hoisting System. In Proceedings of the 2018 International Conference on Mechanical, Electronic, Control and Automation Engineering (MECAE 2018), Qingdao, China, 30–31 March 2018; pp. 221–233.
33. Gao, Z.; Kim, Y.; Alley, E.; Wołoszyk, K.; Jiang, Z.; Stanley, A.; Luo, H.; Andric, J.; Caire, M.; Sacchet, A.; et al. Committee II.1: Quasi-Static Response. In *Proceedings of the 22nd International Ship and Offshore Structures Congress*; Springer: Singapore, 2026; pp. 49–67.
34. Yu, Z.; Amdahl, J. A review of structural responses and design of offshore tubular structures subjected to ship impacts. *Ocean Eng.* **2018**, *154*, 177–203. [CrossRef]
35. Mo, Z.; Xie, K.; Zhao, F.; Li, J.; Li, Y. A Small Floating Platform Designed for Unmanned Defense System. *J. Mar. Sci. Eng.* **2023**, *11*, 278. [CrossRef]
36. China Classification Society. *Code of Practice for the Construction of Sea-Going Vessels Under Chinese Navigation*; China Communications Press: Beijing, China, 2024. (In Chinese)
37. Matusiak, J. *Dynamics of a Rigid Ship*; Aalto University: Espoo, Finland, 2017.
38. Eyres, D.J.; Bruce, G.J. *Ship Construction*; Elsevier: Amsterdam, The Netherlands, 2012.
39. International Maritime Organization. *International Code on Intact Stability, 2008 (2020 Edition)*; International Maritime Organization: London, UK, 2020.
40. Brandt, A. *Noise and Vibration Analysis: Signal Analysis and Experimental Procedures*; Wiley & Sons: Hoboken, NJ, USA, 2010.